

A comparison of the intensity scaling for nonlinear Compton scattering and bremsstrahlung x-ray emission

Christina Ingleby¹, Stuart Morris², Christopher Arran¹, Christopher Ridgers¹, and Kate Lancaster¹

¹*York Plasma Institute, University of York, York, UK*

²*Department of Physics, University of Warwick, Coventry, UK*

Abstract

Ultraintense laser-plasma experiments generate a variety of high-energy radiation including nonlinear inverse Compton scattered (NCS) x-rays which are expected to be a key experimental observable as we transition into the QED plasma regime. However, there is also a high bremsstrahlung x-ray background that reduces our ability to observe NCS x-rays. Previous numerical studies comparing NCS and bremsstrahlung emissions fail to capture the full temporal emission of both processes. We present for the first time 2D PIC and 3D hybrid-PIC EPOCH simulations that capture up to 150 ps of the laser-plasma interaction and directly compare the NCS and bremsstrahlung emission for a plastic target for intensities of $10^{20} - 10^{23} \text{ W/cm}^2$. We present angular distribution plots where the NCS emission is seen to dominate at intensities greater than $5 \times 10^{21} \text{ W/cm}^2$ and the target design is seen to successfully divert the bremsstrahlung signal away from the NCS lobe regions, making the possibility of experimental observation of NCS at lower intensities more likely.

Keywords: High-power laser; high-intensity; x-rays; nonlinear inverse Compton scattering; bremsstrahlung

1. Introduction

With the commissioning of new multi-PW laser facilities, laser intensities beyond 10^{22} W/cm^2 are now achievable and open new avenues for investigating high-intensity laser-plasma interactions. These lasers produce strong electromagnetic (EM) fields that accelerate electrons in solid targets to ultra-relativistic energies. As the strength of the electric field approaches the Schwinger limit ($E_S = 1.32 \times 10^{18} \text{ V/m}$), the electrons become more relativistic and radiate a significant portion of their energy as x-ray (gamma-ray) photons^[1–4]. The ratio of the laser field compared to the Schwinger limit in the rest frame of the relativistic electrons is defined as the electron quantum parameter χ_e . It is given by Equation (1); here χ_e depends on the components of the electric field of the laser (\mathbf{E}_\perp and E_\parallel), the velocity of the electrons (\mathbf{v}_e), the magnetic field of the laser (\mathbf{B}), and the electron Lorentz factor (γ_e).

$$\chi_e = \frac{\gamma_e}{E_S} \sqrt{(\mathbf{E}_\perp + \mathbf{v}_e \times \mathbf{B})^2 + E_\parallel^2 / \gamma_e^2} \quad (1)$$

When the electron quantum parameter $\chi_e > 0.1$, quantum and relativistic effects become important and influence classical plasma processes, generating a quantum electrodynamic (QED) plasma^[5]. QED plasmas are predicted to produce intense high-energy radiation, such as hard x-

ray bursts through non-linear inverse Compton scattering (NCS)^[6]. NCS x-rays are produced when multiple low-energy photons interact with an electron in the presence of a strong electromagnetic field, producing a high-energy photon as a result^[7]. High-energy NCS photons also produce electron-positron pairs through the nonlinear Breit-Wheeler (NLBW) process^[8]. NCS x-rays, electron-positron pairs, and high-energy ions are all relevant to a wide range of applications including radiography, radiotherapy^[9], laboratory astrophysics, and fast ignition fusion schemes^[10,11].

Previous simulation work has indicated that the intense bursts of NCS x-rays are a key observable when we transition into the QED plasma regime^[12]. However, at currently achievable laser intensities of 10^{20} Wcm^{-2} – 10^{22} Wcm^{-2} , the additional x-ray emission process of bremsstrahlung emission is also present and generates x-rays that are currently indistinguishable from NCS x-rays^[13]. NCS x-rays are rarely observed unambiguously at current laser intensities due to the high bremsstrahlung background produced from laser-plasma interactions. Recent work^[14] has shown that it is possible to estimate the bremsstrahlung background by completing a target thickness scan.

With the advancement of laser technology, it is expected that we will soon be able to probe the QED plasma regime experimentally, but this is complicated by the presence of a high bremsstrahlung background that obscures the key

Correspondence to: Christina Ingleby Email: christina.ingleby@york.ac.uk

observable NCS x-rays. Therefore, methods of reducing the high bremsstrahlung background must be employed. Previous work^[15–19], has highlighted areas of high electron-to-photon conversion efficiency, showing that bremsstrahlung emission depends on parameters such as target composition and density, target thickness, and laser intensity. They show that bremsstrahlung emission can be reduced by using a thin target with a low atomic number (Z) for all currently achievable laser intensities. Using a thin, low- Z target will result in the majority of the electron energy being radiated away by electrons refluxing between the target boundaries.

Many other simulation studies^[20–23] have been conducted that compare the scaling of both NCS and bremsstrahlung emission with peak laser intensity, target thickness, or target composition. However, most of these studies have been conducted on multi-fs timescales. As the signal from NCS x-rays can be confounded by bremsstrahlung radiation, any simulation studies must consider the full bremsstrahlung emission. Previous work^[15,24] has shown that refluxing electrons can produce bremsstrahlung radiation on a multi-ps timescale that is often neglected in simulation studies. We anticipate that bremsstrahlung emission will dominate at lower intensities, and NCS will become prominent at intensities above 10^{22} Wcm^{-2} ^[25]. However, the scaling of both emissions with intensity on a multi-ps timescale has not been thoroughly investigated. We have limited knowledge of where the crossover between the dominant emission occurs for scenarios where bremsstrahlung reduction methods and longer simulation timescales are considered.

In this paper, we present the results from novel 2D particle-in-cell (PIC) and 3D hybrid-PIC EPOCH^[26] simulations investigating the intensity scaling of bremsstrahlung and NCS x-rays on a multi-ps timescale. We have calculated the x-ray conversion efficiencies (η) of both populations. The simulations directly compare the NCS and bremsstrahlung emission using a low- Z solid target of dimensions $10.5 \mu\text{m} \times 1\text{mm} \times 1\text{mm}$. The laser intensity was increased from $1 \times 10^{20} \text{ W/cm}^2$ to $1 \times 10^{23} \text{ W/cm}^2$ to capture the full intensity range available at current facilities. This corresponds to a χ_e range of approximately $2.5 \times 10^{-4} - 0.13$ so we can expect quantum effects to be present at higher intensities.

2. Methodology

The main objective of the simulations presented in this paper is to investigate the intensity scaling of both NCS and bremsstrahlung x-ray emission and to demonstrate whether detecting NCS emission is viable at current facilities. The work in this paper uses both the particle-in-cell (PIC) code EPOCH^[26] and its hybrid-EPOCH^[15] counterpart, which only considers fast electrons accelerated by the laser at the target's front surface moving through a static background representing the colder bulk target. Simulating laser-plasma interactions using PIC codes provides a useful tool for physics investigations, but is very computationally

expensive, particularly when studies need to be conducted on multi-ps timescales. The hybrid-EPOCH counterpart is more computationally efficient, so it can be run on a multi-ps timescale in 3D on clusters with only a few hundred processors.

Hybrid-EPOCH uses electron injection to model the interaction with the laser pulse and the injected electron properties are based on supposed laser conditions. It can model the evolution of currents and fields within the target due to the motion of the electrons such as resistivity and Ohmic heating. The hybrid routines also include scattering and collisions between electrons and ions such as ionisation loss and Moller scatter. Additional routines include the Photoelectric effect and $K\text{-}\alpha$ emission. However, as the code tracks the evolution of parameters only within the target, it is not capable of determining external fields around the target such as sheath fields. In laser-plasma interactions, electrons are accelerated through the target and leave the bulk material on a faster timescale than the acceleration of ions. This creates a charge separation and produces a sheath field around the target that acts to accelerate the ions in a process called target normal sheath acceleration (TNSA)^[27]. The generation of the sheath field around the target can cause the refluxing of electrons back into the target. In laser-plasma simulations, fast electrons can escape the simulation window through any of the x , y , and z boundaries if they possess sufficient energy to overcome the sheath field surrounding the target. Since hybrid-EPOCH cannot model sheath fields, instead the simulation boundaries can be modified to allow for electrons to escape or reflux back into the target to model the effects of a sheath field. The escape kinetic energy value associated with the TNSA boundaries can be scaled using $\kappa_{esc} a_0 m_e c^2$, electrons that have energies higher than the escape kinetic energy will leave the simulation window. If electrons do not have sufficient energy to escape then they will be refluxed back into the target and will undergo a momentum loss to the sheath field as a result. The momentum loss can be scaled using $\kappa_{tnsa} a_0 m_e c$. When electrons are refluxed back into the target they will be scattered and their trajectory will be modified by some angle $\sigma_{\Delta\theta}$. These scaling laws are taken from a previous study on reflux characteristics in 2D PIC simulations^[15?] and have been benchmarked against experiments for laser intensities between $1 \times 10^{20} - 22 \text{ W/cm}^2$. Values for the TNSA boundary characterisation parameters κ_{esc} , κ_{tnsa} and $\sigma_{\Delta\theta}$ were also determined for different targets at varying intensities.

The methodology used is shown in Figure 1 and shows a two-stage simulation setup where the laser-plasma interaction is separated. The first step is a 2D EPOCH simulation that captures the laser interaction with the preplasma and front surface of the target. The 2D simulation is run on a femtosecond timescale to allow sufficient temporal resolution to capture the full NCS x-ray emission generated. In EPOCH, QED processes such as NCS photon emission,

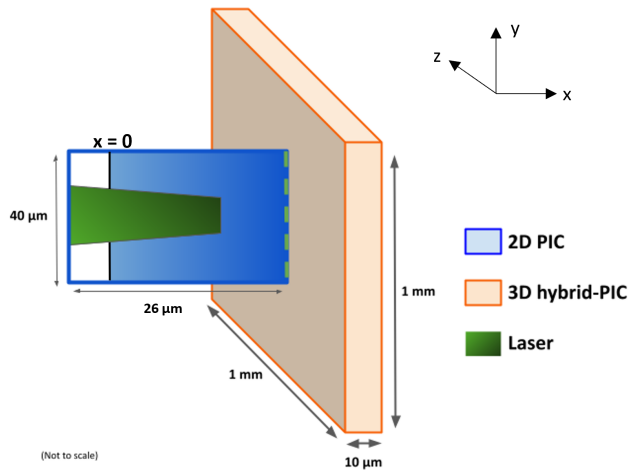


Figure 1. Schematic of the simulation methodology employed in this paper. The blue rectangle represents the 2D EPOCH simulation domain including a laser and a pre-plasma density gradient. The $x = 0$ point where the density gradient begins is marked by a solid, black line within the blue rectangle. The green dashed line represents the probe plane that captures electrons leaving the pre-plasma and entering a target. The orange cuboid represents the simulation domain of the 3D hybrid-EPOCH simulation. The TNSA x , y and z boundaries are attached to each face of the orange cuboid within the simulation domain.

radiation reaction, and pair production are modelled using Monte Carlo emission algorithms^[29,30] within the QED module. Multiple species of photons can be initialised independently in the input deck using the identify tag in each photon species block. This will generate individual outputs for each photon species, including NCS and bremsstrahlung photons. A probe plane is placed behind the front surface of the target to capture the properties of the accelerated electrons as they begin to move through the target material. These electrons are then characterised and converted into a hot electron population that can be injected into a hybrid-EPOCH simulation. The electrons are converted to injectors by assuming cylindrical symmetry and randomly selecting an injection angle between $\pm\pi/2$ to rotate the position and momenta of each electron from the 2D output in the y , z plane. This ensures that the electrons are injected within a 3D cone. The particle weight of each electron is then also modified to include the rotation angle and conserve number density within each grid cell. The modified electron population is then injected into a 3D hybrid-EPOCH simulation that captures hot electrons as they traverse the target material, producing bremsstrahlung x-rays as they interact with the background target nuclei. This simulation is run on a multi-ps timescale to ensure that the full bremsstrahlung emission is captured.

The 2D EPOCH simulations used a spatial grid of $26\ \mu\text{m} \times 40\ \mu\text{m}$ with a grid cell size of 20 nm. The target had y dimensions of $30\ \mu\text{m}$ and a solid thickness of $0.5\ \mu\text{m}$. The simulations used a CH plastic foil target (polypropylene)

Table 1. Table of the relativistically corrected critical density ($n_{crit,\gamma}$) for each simulation presented in this paper and the subsequent range of density in the pre-plasma in units of $n_{crit,\gamma}$.

Intensity (W/cm^2)	$n_{crit,\gamma}$ (m^{-3})	Pre-plasma density
1×10^{20}	6.82×10^{27}	6 - 42 $n_{crit,\gamma}$
5×10^{20}	1.51×10^{28}	3 - 19 $n_{crit,\gamma}$
1×10^{21}	2.13×10^{28}	2 - 14 $n_{crit,\gamma}$
3×10^{21}	3.68×10^{28}	1 - 8 $n_{crit,\gamma}$
5×10^{21}	4.76×10^{28}	0.8 - 6 $n_{crit,\gamma}$
1×10^{22}	6.73×10^{28}	0.6 - 4 $n_{crit,\gamma}$
5×10^{22}	1.50×10^{29}	0.3 - 2 $n_{crit,\gamma}$
1×10^{23}	2.13×10^{29}	0.2 - 1 $n_{crit,\gamma}$

with an electron density of $2.9 \times 10^{29}\text{m}^{-3}$, which is approximately $240n_{crit}$ (the classical critical density is $1.2 \times 10^{27}\text{m}^{-3}$). However, the electrons within the simulations will travel at relativistic velocities, so we need to consider the relativistically corrected critical density $n_{crit,\gamma}$. Table 1 contains $n_{crit,\gamma}$ for the laser intensities investigated in this paper. An exponential pre-plasma was attached to the front surface of the target using a density profile of the form $n_e = n_e e^{(x-20\mu\text{m})/10\mu\text{m}}$ from the $x = 0$ line until the position of the probe plane in Fig. 1. The pre-plasma density range for each simulation is given in Table. 1 in units of $n_{crit,\gamma}$. For laser intensities $> 5 \times 10^{21}\text{W}/\text{cm}^2$, some proportion of the pre-plasma will be relativistically underdense and transparent to the laser. Previous studies^[31–34] have shown that NCS emission is enhanced in regions of relativistically underdense plasmas and including a pre-plasma with a long scale length can increase the NCS conversion efficiency. We have included long-scale length pre-plasma within the simulations but the effects of relativistic transparency are not directly studied within this paper.

The bulk C^{6+} and H^+ ion densities were set to 1/8 and 1/4 of the electron density respectively. A second edge population of electrons, C^{6+} and H^+ ions, was used to avoid the draining of particles due to open boundaries within the simulation. These populations were confined to $x > 20.5\ \mu\text{m}$ and $|y| > 15\ \mu\text{m}$ with their x -max, y -min and y -min boundaries set to reflective. The initial electron and ion temperatures were set to 1 keV for all simulations. These initial temperatures are insignificant compared to the heating from the laser even in the early stages of the interaction. For simulations below $5 \times 10^{22}\text{W}/\text{cm}^2$, 300 particles per cell (ppc) were used for all ion and electron species. 100 ppc was used for $5 \times 10^{22}\text{W}/\text{cm}^2$ and 20 ppc was used for $1 \times 10^{23}\text{W}/\text{cm}^2$. Convergence tests were conducted at these intensities to evaluate the impact of changing the number of ppc and were found to have a negligible impact. To mitigate unphysical heating in the simulations, current smoothing was used alongside a 5th-order particle shape (BSPLINE3). A

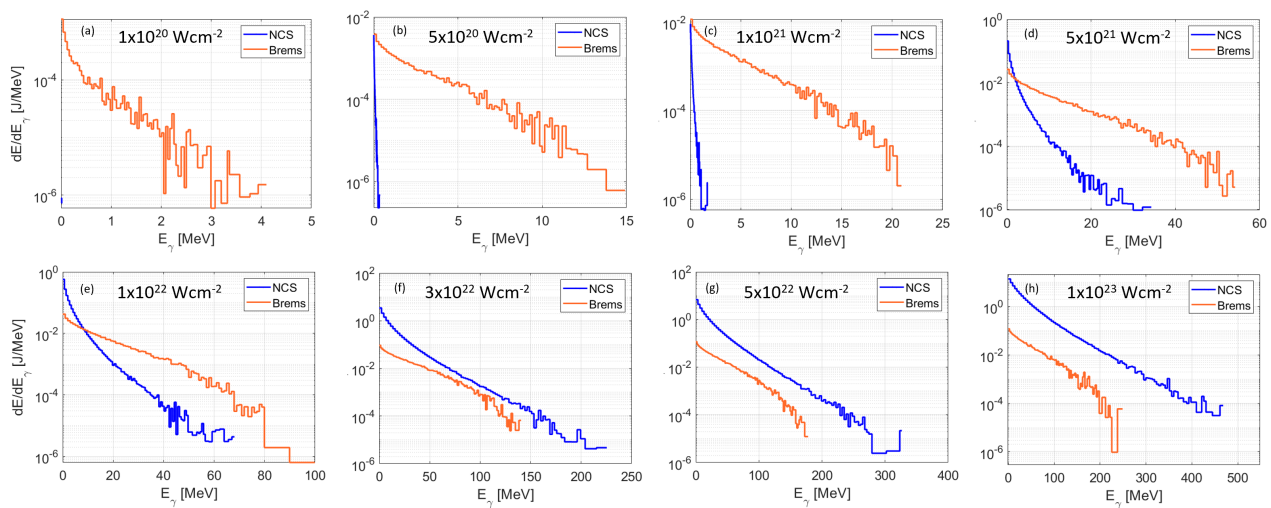


Figure 2. X-ray photon energy spectra of NCS (blue) and bremsstrahlung (orange) populations from EPOCH simulations for increasing laser intensity up to $1 \times 10^{23} \text{ W/cm}^2$. Note that the axes on the spectra change as the intensity increases to ensure that all of the data can be seen.

1 μm wavelength laser pulse was focused onto the target surface from the minimum x-boundary at normal incidence. The laser had a Gaussian spatial and temporal profile with FWHM of 5 μm and 40 fs respectively.

The 3D hybrid-EPOCH simulations used a spatial grid of $10\mu\text{m} \times 1\text{mm} \times 1\text{mm}$ with cell sizes of 70nm. The carbon and hydrogen densities were set to $3.9 \times 10^{28}\text{m}^{-3}$ and $7.7 \times 10^{28}\text{m}^{-3}$ respectively. Hybrid-EPOCH assumes a background electron density to enforce neutrality within the bulk target. Any fast electrons that are injected into the simulation will be a small perturbation on top of the assumed electron target density. The initial ion temperatures were set to 300K (equivalent to $26 \times 10^{-3}\text{keV}$) for both species to simulate a cold, dense target. TNSA boundaries were used for both the min and max x, y and z boundaries using the following parameter values; $\kappa_{esc} = 2$, $\kappa_{tnsa} = 2.7 \times 10^{-3}$ and $\sigma_{\Delta\theta} = \pm 23$. These are typical values taken from the previous study on refluxing^[152]. To ensure the full bremsstrahlung emission was captured, the 3D simulations were run for 125 ps.

3. Results

3.1. Energy spectra

The x-ray photon energy spectra can be seen in Figure 2 and have been plotted using a logarithmic histogram. The data presented in the spectra have been integrated over the entire angular distribution of x-rays. The spectra show low noise for lower photon energies at all intensities, but high shot noise for higher energies. This is to be expected as we anticipate that fewer high-energy photons will be present, but it does present some uncertainty in the results for higher photon energies. For example, in Figure 2(g) there is a small increase in the NCS signal above 300 MeV, however, this is

most likely a result of noise in the simulation and will be neglected.

Figure 2 shows that bremsstrahlung emission dominates the energy spectra at most intensities. At lower intensities between 1×10^{20} and $5 \times 10^{21} \text{ W/cm}^2$, bremsstrahlung emission dominates at most photon energies, particularly at higher energies up to around 50 MeV. However, Figure 2(a) indicates that most of the population is composed of sub-1 MeV photons. The bremsstrahlung emission continues to dominate at higher energies until $3 \times 10^{22} \text{ W/cm}^2$, where NCS dominates the entire energy spectrum. Figure 2 indicates that there is a small increase in the total energy and flux of bremsstrahlung emission after NCS dominates the spectrum. This can also be seen in Figure 3, a comparison of the bremsstrahlung spectra at some of the highest laser intensities. We can also see that bremsstrahlung emission scales with intensity, however, the change in the total flux and energy decreases as the intensity increases.

Figures 2(a-c), show that the NCS photon population has a significantly lower flux and lower total energy than the bremsstrahlung emission and the NCS signal is barely visible on the spectra. We anticipate that NCS scales with the laser intensity, and this can be seen from the increase in NCS photon flux and energy as the intensity increases. Figures 2(d and e) show an increase in the overall NCS photon signal, particularly at lower energies where the signal is higher than bremsstrahlung, although it is not clear at what energies the NCS signal is higher. When comparing NCS and bremsstrahlung photons directly for all energies, it is difficult to see at which energies NCS dominates the spectra at lower intensities. Figure 4 shows spectra for $5 \times 10^{21} \text{ W/cm}^2$ and $1 \times 10^{22} \text{ W/cm}^2$ that have been zoomed in to show photon energies of 0 - 10 MeV. Figure 4(a) shows that the NCS population dominates the photon spectra for energies up to

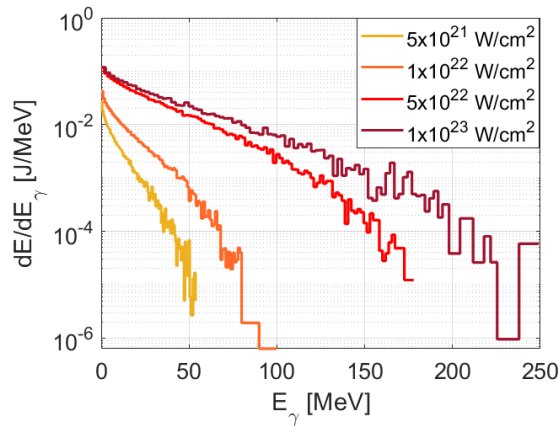


Figure 3. A comparison of the bremsstrahlung energy spectra produced from the four highest laser intensities.

2 MeV and 4(b) dominates up to 10 MeV. These suggest that the NCS photon population consists of a large number of lower-energy photons. In an experimental setting, it would be prudent to focus our attention on characterising the lower end of the photon spectra where NCS is much more abundant than bremsstrahlung. This could be done using photon spectrometers that have high-energy resolution below 10 MeV.

At $3 \times 10^{22} \text{ W/cm}^2$, NCS dominates the spectra at all intensities with photon fluxes at least one to two orders of magnitude higher than bremsstrahlung and includes photon energies up to 300 MeV. This crossover point where NCS dominates is an order of magnitude higher than previous estimates using a $2 \mu\text{m}$ thick CH target^[22]. We expect that our estimate is higher due to using a thicker target and modelling the bremsstrahlung emission up to 125 ps. Previous work has compared NCS and bremsstrahlung on similar timescales, but this does not capture the full bremsstrahlung emission that will be produced in an experimental setting. It is possible to distinguish between NCS and bremsstrahlung temporally, but this would require further development of sub-ps photon diagnostics that could provide the necessary temporal resolution (multi-fs) in this instance.

3.2. Angular emission

The photon spectra disguise features that can be measurable in real experiments, where detectors only capture particles emitted in a small angular range. The angular distribution of x-ray energy for NCS and bremsstrahlung emission is shown in Figure 5. Here the x-ray energy per radian in the plane ($dE/d\theta$) is plotted to allow a direct comparison between the two x-ray populations. The characteristic lobe shape of the NCS emission is seen at $\theta = 45^\circ$ and $\theta = 315^\circ$, or $\pm 45^\circ$ from the laser propagation axis and is predominantly in the forward direction, which is consistent with previous studies on NCS emission^[5,34]. However, other previous

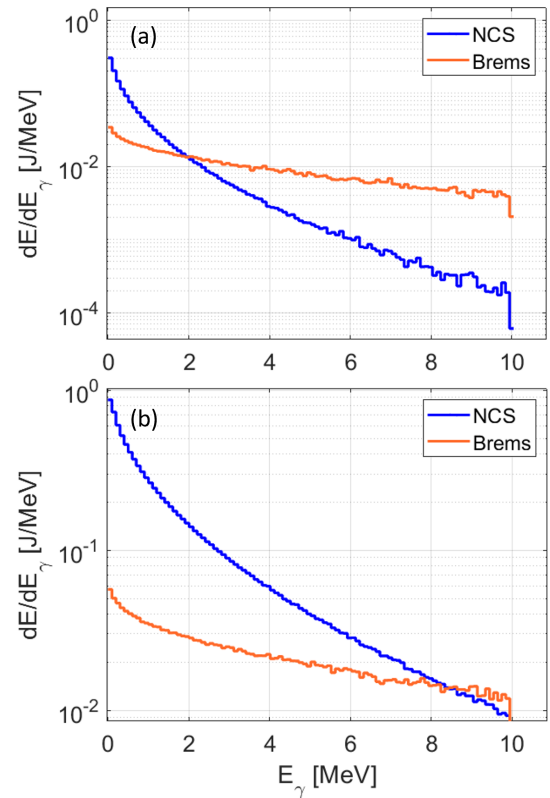


Figure 4. Comparison of the energy spectra for photons between 1 keV and 10 MeV for intensities of a) $5 \times 10^{21} \text{ W/cm}^2$ and b) $1 \times 10^{22} \text{ W/cm}^2$.

studies indicate that these lobes are centred at $\pm 30^\circ$ from the laser propagation axis.

NCS emission is small compared to bremsstrahlung emission for intensities up to $5 \times 10^{21} \text{ W/cm}^2$ but becomes the dominant emission at higher intensities. There is a crossover between 5×10^{21} and $1 \times 10^{22} \text{ W/cm}^2$ where NCS begins to dominate, and the emission becomes significantly more prominent at $1 \times 10^{22} \text{ W/cm}^2$. It is much easier to see where NCS begins to dominate in the angular profiles than in the energy spectra of Figure 2. Above $1 \times 10^{22} \text{ W/cm}^2$ there is some backwards emission (towards $\theta = 180^\circ$) which may be consistent with re-injected electron synchrotron emission (RESE)^[31] or transversely oscillating electron synchrotron radiation (TOEE)^[35]. Both processes generate photon emission in the backward direction towards the laser pulse. RESE occurs predominantly in underdense plasma such as that present in the long-scale-length pre-plasma whereas TOEE occurs in plasma close to near-critical density. The backwards emission increases with intensity and at $3 \times 10^{22} \text{ W/cm}^2$, the backwards emission appears to be greater than the forward emission. The backwards emission at $1 \times 10^{23} \text{ W/cm}^2$ appears to be of a similar magnitude to the forward emission. However, the evolution of the characteristic lobes requires further investigation. Figure 6 shows the angular distribution for NCS x-rays with KE > 50 MeV and KE

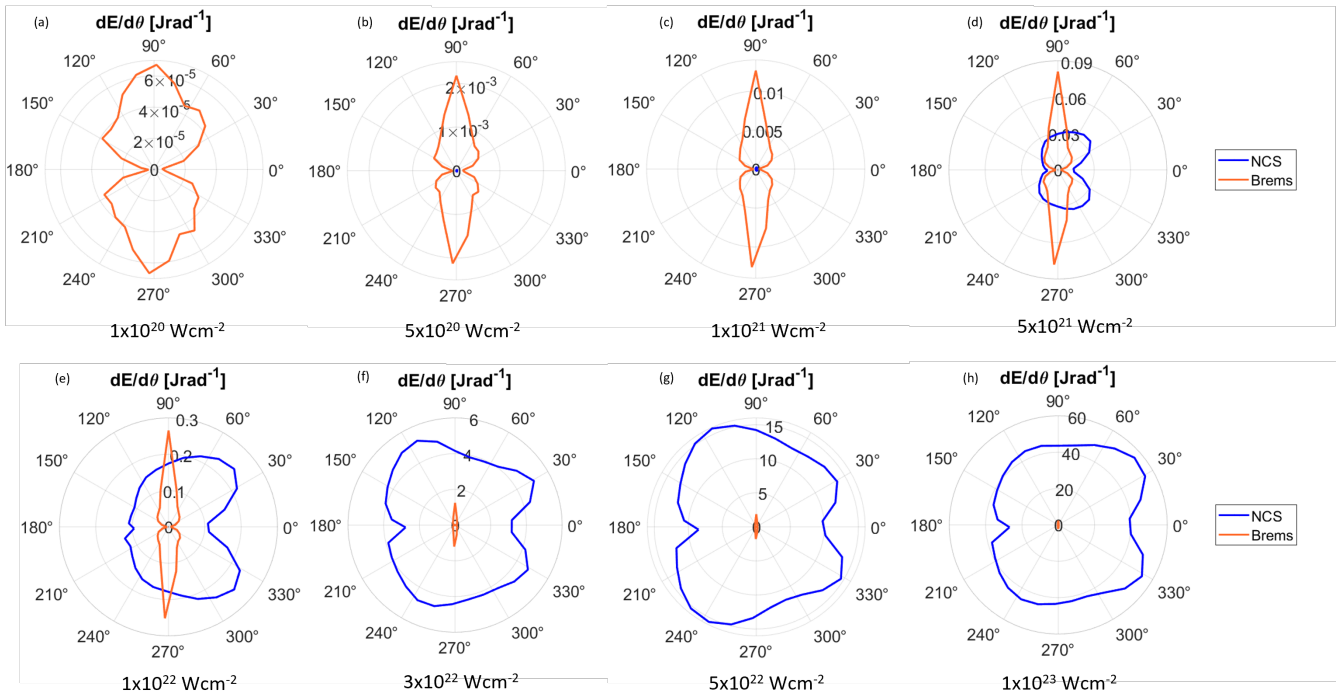


Figure 5. 2D angular x-ray energy distribution comparison for NCS (blue) and bremsstrahlung (orange) for the intensity range 10^{20} - 10^{23} W/cm². The laser propagation direction is along the $\theta = 0^\circ$ axis. Note that the axes on these figures change as the intensity increases to ensure that all of the data can be seen.

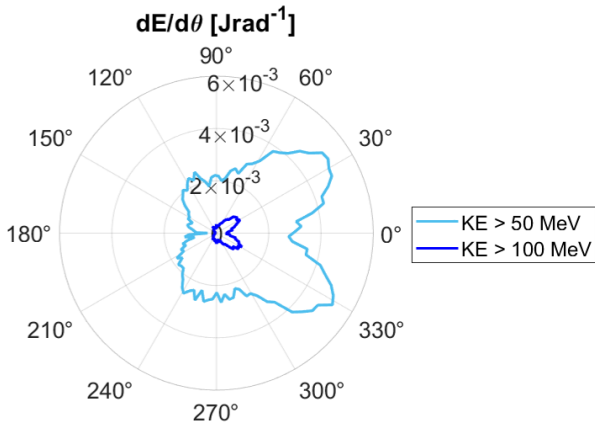


Figure 6. 2D angular energy distribution plot with energy contours for NCS x-ray energies > 50 MeV (light blue) and > 100 MeV (dark blue) for 10^{23} W/cm².

> 100 MeV for 10^{23} W/cm². The characteristic lobes are still present for higher photon energies but peak at $\pm 30^\circ$ so the lobes are likely being obscured by an abundance of lower energy photons in Figure 5. There is still some backwards emission present within the 50 MeV contour which indicates that the backwards emission does not only consist of lower energy photons. However, the majority of emissions for these energy contours are in the forward direction as expected.

Bremsstrahlung emission dominates at lower intensities as expected, with the emission becoming more prominent at $\theta = 90^\circ$ and $\theta = 270^\circ$ with increasing intensity. These results are similar to previous studies^[13,15] that showed that the angular distribution of bremsstrahlung radiation was affected by changes in the electron momentum components p_x and p_y as they reflux across the sheath fields around the target. In the simulations conducted within this paper, when electrons move across the TNSA boundaries they lose energy and momentum due to scattering and so will re-enter the solid with less momentum and energy. We can expect that electrons that pass across the TNSA boundaries more frequently will lose more energy, and thus cannot radiate as much energy through bremsstrahlung emission as they traverse the target. This is the case for electrons moving longitudinally through the target along the laser axis direction as they come into contact with the TNSA x-boundaries more frequently. However, since the target has a larger transverse length, this allows electrons to lose more of their energy through bremsstrahlung radiation before passing through the TNSA y and z-boundaries^[24]. This produces significant bremsstrahlung emission perpendicular to the laser axis and is directed away from the NCS lobes. Since there is a distinction between the angular emission of both processes, placing x-ray detectors at $\pm 45^\circ$ on either side of the laser axis would increase the possibility of observing NCS experimentally at current facilities.

Figure 7 shows the comparison between the energy spectra

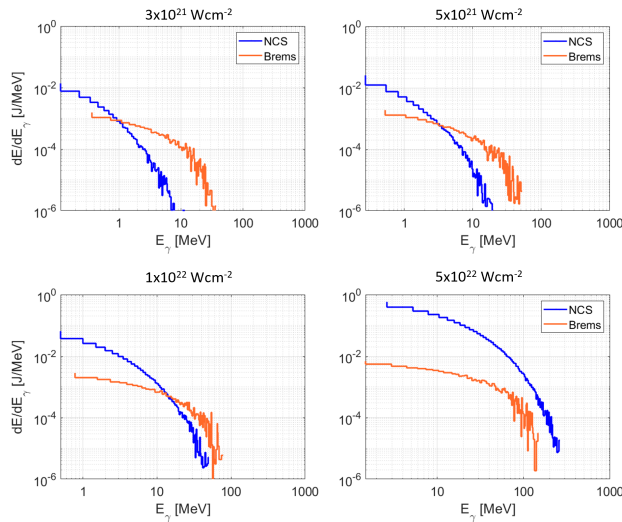


Figure 7. A comparison of the photon spectra for $10^{21} - 10^{22}$ W/cm² between an angle of 30° and 60° from the laser propagation axis. The axes have been fixed for comparison and are on a log scale.

for NCS and bremsstrahlung x-rays for angles between 30 and 60° from the laser propagation axis for intensities between $10^{21} - 10^{22}$ W/cm². It shows the energy spectra we could expect to see by placing a detector within the region where the NCS lobes are most prominent. It indicates that we can observe the NCS signal above the bremsstrahlung background for mid-range intensities in multiple energy ranges. Figures 7(a) and (b) show that there is a prominent NCS signal in the keV range that is not apparent in Figures 2(d) and (e). This extends to the low MeV range for intensities of mid- 10^{21} and low- 10^{22} . As anticipated, the NCS signal completely dominates the bremsstrahlung signal at intensities of mid- 10^{22} .

3.3. Conversion efficiency

The laser-to-NCS photon conversion efficiencies (η_{NCS}) and bremsstrahlung conversion efficiencies (η_{br}) were calculated and are presented in Figure 8(a). Overall, both efficiencies increase with the laser (I_L), it is clear that NCS emission scales more rapidly with intensity than bremsstrahlung emission so different scaling laws have been applied. A second-order polynomial fit has been used to determine that η_{NCS} scales with I^2 , whereas a first-order polynomial was used to determine the η_{br} scaling (approx. $0.5I_L$). Previous studies^[31] have suggested that the power radiated when electrons collide with a counter-propagating laser pulse scales with $\gamma^2 E^2$. It is known that laser intensity scales with E^2 so the power radiated by electrons can be assumed to scale with I^2 . This NCS scaling law is consistent with other studies conducted^[22,23,25] that suggest ranges of $\eta_{NCS} \propto I^{1.25-2}$. Bremsstrahlung emission is expected to scale linearly with the hot electron energy and thus, with

the laser energy. For the simulations in this paper, we have adjusted the laser intensity by linearly increasing the energy in the beam, therefore, a linear scaling law is justified. The scaling law used for bremsstrahlung is consistent with other studies conducted in the literature which suggest possible intensity scaling laws of $\eta_{br} \propto I^{0.5-1}$ [13,19].

Figure 8(a) shows that η_{NCS} increases with laser intensity, reaching a peak at 34.81% for 1×10^{23} W/cm². This is comparable to previous estimates^[5,12,25,34,36] of 3-40% for laser intensities of up to 5×10^{23} W/cm². These previous studies have also shown that target properties such as density and pre-plasma scale length have a significant impact on photon conversion efficiencies. There is a transition from a bremsstrahlung-dominated regime ($1 \times 10^{20} - 5 \times 10^{21}$ W/cm²) to an NCS-dominated regime ($> 5 \times 10^{21}$ W/cm²) as the laser intensity increases. The crossover around 5×10^{21} W/cm² is present and consistent with other results presented in this paper.

The bremsstrahlung conversion efficiency η_{br} is higher than η_{NCS} at lower intensities and peaks at 0.68% for 3×10^{22} W/cm², which is less than previous estimates^[15]. However, the target consists of lower Z material and has a smaller volume than the targets used in those estimates so we expect the conversion efficiency to be smaller. A linear scaling law has been applied to the bremsstrahlung conversion efficiency in the form $\eta_{br} \propto 0.5I_L$. The scaling law is shown to be a good fit to the data for intensities up to 1×10^{22} W/cm², after which η_{br} plateaus as we enter the NCS-dominated regime. There is also a decrease in η_{br} at 1×10^{23} W/cm² compared to η_{br} at 3×10^{22} W/cm² and 5×10^{22} W/cm². A plateau and decrease in η_{br} at high intensities could be due to QED effects such as radiation reaction as electrons are producing a high flux of high-energy photons. This will result in a decrease in the total energy of the electron population traversing the target producing bremsstrahlung photons.

To determine whether the decrease in η_{br} is due to NCS and QED effects, 3 additional simulations were run with identical parameters except for the absence of the QED module. Turning off the QED module ensures that the simulation runs without NCS emission and reduces the radiation reaction effect on electrons, producing more high-energy electrons that traverse through the solid. Figure 8(b) shows the electron energy spectra containing the population of electrons that were injected into the 3D hybrid-EPOCH simulation for 1×10^{23} W/cm². There is a significant difference in the injected electron population when the QED module is turned off; the population of higher energy electrons increases up to energies of 900 MeV, as opposed to 500 MeV when the QED module is used. The total electron energy injected also increases significantly (x3) when the QED module is turned off. The difference in the electron spectra will be due to radiation reaction effects as the electron population produces NCS photons earlier in the interaction.

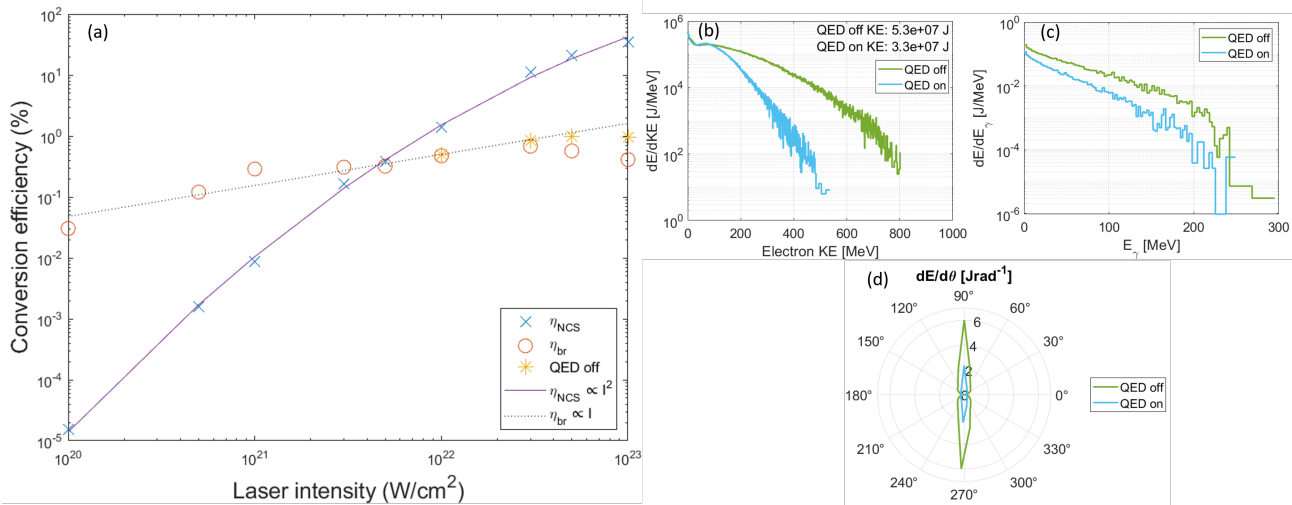


Figure 8. (a) intensity scaling of the energy conversion efficiencies of laser-NCS x-rays and hot electron-bremsstrahlung x-rays, (b) a comparison of the electron energy spectra produced from the electron injectors for 1×10^{23} W/cm² when the QED module is on and off, (c) bremsstrahlung energy spectra for 1×10^{23} W/cm² when the QED module is on and off, (d) bremsstrahlung angular energy plot for 1×10^{23} W/cm² when the QED module is on and off.

The reduction in high energy electrons reduces the rate of bremsstrahlung emission as shown in Figure 8(c) and (d), which show the difference in the bremsstrahlung energy spectra and angular emission due to QED effects. Both the energy spectra and the angular emission are enhanced when there are no QED effects. These simulations are shown by the points 'QED off' in Figure 8. There is no difference between the η_{br} values at 1×10^{22} W/cm². Still, there is a non-negligible difference at higher intensities indicating that NCS and QED effects begin to have a significant impact on bremsstrahlung emission at 5×10^{22} W/cm². As more energy is being transferred to the NCS population and high-energy photons are produced, the effects of radiation reaction on the electrons are greater which means less energy is available to the bremsstrahlung population. The 'QED-off' simulations still indicate a plateau in η_{br} after 5×10^{22} W/cm² but this is less significant; η_{br} is 0.98% and 1.07% for QED-off simulations compared to 0.57% and 0.41% for the original simulations. We have noted that there is a difference in the flux and total energy of the injected electron species when the QED module is turned off which can explain the increase in η_{br} , however, it does not explain the presence of the plateau. An additional consideration to make is the effect of the sheath boundaries implemented in the 3D hybrid-PIC simulations. The escape energy values are scaled with laser intensity to ensure that electrons with sufficiently high-energy can escape the target and simulation window. Those that do not possess sufficiently high-energy lose energy to the boundaries and are refluxed back into the target. However, an increase in the total energy and flux of the electron population when the QED module is turned off has not been accounted for and a higher number of electrons could be escaping through the back of the

target. A consequence of this is that the very-high-energy electrons could pass through the material without refluxing and interacting with the target material multiple times. This could cause an apparent plateau and decrease in η_{br} since an increase in laser intensity does not generate an increase in bremsstrahlung photons.

4. Conclusions

The scaling of NCS and bremsstrahlung x-ray emission in the intensity range 1×10^{20} - 1×10^{23} W/cm² has been investigated by conducting 2D PIC and 3D hybrid-PIC EPOCH simulations. For intensities $< 5 \times 10^{21}$ W/cm² it was found that bremsstrahlung emission generates more photon energy and dominates both the angular energy distribution and the energy spectra. However, the work conducted within this paper suggests that there is a crossover between the dominant emission mechanism occurring at 5×10^{21} W/cm² where NCS emission dominates. Here NCS emission produces a higher total photon energy and dominates the angular energy distribution. The characteristic NCS lobe shapes were observed on the angular distribution plots for all intensities at $\pm 45^\circ$ from the laser propagation axis. These results suggest that the angular emission of NCS and bremsstrahlung emission are prominent in different directions and can be exploited experimentally. From the simulations conducted, we found a maximum NCS conversion efficiency (η_{NCS}) of 34.81% for 1×10^{23} W/cm² compared to a maximum bremsstrahlung conversion efficiency (η_{br}) of 0.68% for 3×10^{22} W/cm². We noted a plateau in the bremsstrahlung conversion efficiency at high-intensities and investigated whether it was a result of increased radiation reaction effects as we enter the NCS-dominated regime. Further work on

this includes demonstrating these findings experimentally at a high-power laser facility which can achieve intensities above 10^{22} W/cm². These effects should be measurable in upcoming experiments, which could observe non-linear inverse Compton scattering above the bremsstrahlung background and potentially show the impact of radiation reaction on bremsstrahlung emission.

Acknowledgements

The authors would like to thank the Science and Technology Facilities Council and the Engineering and Physical Sciences Research Council for their funding towards this project, and the continued support of research into QED laser-plasma physics. We acknowledge funding from the Engineering and Physical Sciences Research Council [EP/S022430/1]. All simulations within this paper were conducted on the Viking HPC supercomputer cluster at the University of York. We are grateful for computational support from the University of York High-Performance Computing Service, Viking and the Research Computing team.

References

1. Antonio Di Piazza, C. Muller, Karen Z. Hatsagortsyan, and Christoph H. Keitel, "Extremely high-intensity laser interactions with fundamental quantum systems", *Rev. Mod. Phys.* **84**, 3 (2012), DOI: <https://doi.org/10.1103/RevModPhys.84.1177>.
2. Mattias Marklund and Padma K. Shukla, "Nonlinear collective effects in photon-photon and photon-plasma interactions", *Rev. Mod. Phys.* **78**, 2 (2006), DOI: <https://doi.org/10.1103/RevModPhys.78.591>.
3. Evgeny N. Nerush, Igor Yu. Kostyukov, L. Ji, and Alexander Pukhov, "Gamma-ray generation in ultrahigh-intensity laser-foil interactions", *Phys. Plasmas* **21**, 013109 (2014), DOI: <https://doi.org/10.1063/1.4863423>.
4. David J. Stark, Toma Toncian, and Alexey V. Arefiev, "Enhanced Multi-MeV Photon Emission by a Laser-Driven Electron Beam in a Self-Generated Magnetic Field", *Phys. Rev. Lett.* **116**, 185003 (2016), DOI: <https://doi.org/10.1103/PhysRevLett.116.185003>.
5. Christopher P. Ridgers, Christopher S. Brady, Roland Ducloux, John G. Kirk, Keith Bennett, Tony D. Arber, Alex P. L. Robinson, and Anthony R. Bell, "Dense Electron-Positron Plasmas and Ultraintense γ rays from Laser-Irradiated Solids", *Phys. Rev. Lett.* **108**, 165006 (2012), DOI: <https://doi.org/10.1103/PhysRevLett.108.165006>.
6. Thomas G. Blackburn, Daniel Seipt, Stepan S. Bulanov, and Mattias Marklund, "Benchmarking semiclassical approaches to strong-field QED: Nonlinear Compton scattering in intense laser pulses", *Phys. Plasmas* **25**, 083108 (2018), DOI: <https://doi.org/10.1063/1.5037967>.
7. C. Bula, Kirk T. McDonald, Eric J. Prebys, Charles Bamber, Steven Boege, Theofilos Kotseroglou, Adrian C. Melissinos, David D. Meyerhofer, W. Ragg, David L. Burke, R. C. Field, Glenn Horton-Smith, Allen C. Odian, J. E. Spencer, Dieter Walz, Steven C. Berridge, William M. Bugg, Konstantin Shmakov, and Achim W. Weidemann, "Observation of Nonlinear Effects in Compton Scattering", *Phys. Rev. Lett.* **76**, 17 (1996), DOI: <https://doi.org/10.1103/PhysRevLett.76.3116>.
8. Christopher S. Brady, Christopher P. Ridgers, Tony D. Arber, and Anthony R. Bell, *Phys. Plasmas* **21**, 033108 (2014), DOI: <https://doi.org/10.1063/1.4869245>.
9. Kenneth W. D. Ledingham and W. Galster, *New J. of Phys.* **12**, 045005 (2010), DOI: <https://doi.org/10.1088/1367-2630/12/4/045005>.
10. Ozgur Culfa and Volkan Sert, *Indian J. Phys.* **94**, 1451–1456 (2020), DOI: <https://doi.org/10.1007/s12648-019-01567-8>.
11. Paul Gibbon and E. Forster, *Plasma Phys. Control. Fusion* **38**, 769 (1996), DOI: <https://doi.org/10.1088/0741-3335/38/6/001>.
12. Christopher P. Ridgers, Christopher S. Brady, Roland Ducloux, John G. Kirk, Keith Bennett, Tony D. Arber, and Anthony R. Bell, *Phys. Plasmas* **20**, 056701 (2013), <https://doi.org/10.1063/1.4801513>.
13. Jiří Vyskocil, Ondřej Klimo, and Stefan Weber, *Plasma Phys. Control. Fusion* **60**, 054013 (2018), DOI: <https://doi.org/10.1088/1361-6587/aab4c3>.
14. Alexander S. Pirozhkov, A. Sagisaka, K. Ogura, E. A. Vishnyakov, A. N. Shatokhin, C. D. Armstrong, T. Zh. Esirkepov, Bruno Gonzalez Izquierdo, T. A. Pikuz, P. Hadjisolomou, M. A. Alkhimova, Christopher Arran, I. P. Tsygvinsev, P. Valenta, S. A. Pikuz, Wei Yan, T. M. Jeong, S. Singh, Ondřej Finke, G. Grittani, M. Nevrlka, C. Lazzarini, A. Velyhan, Takehioto Hayakawa, Yasutaka Fukuda, James K. Koga, Masaya Ishino, Kunitaka Kondo, Y. Miyasaka, Akira Kon, Masaharu Nishikino, Y. V. Nosach, D. Khikhlukha, A. O. Kolesnikov, E. N. Ragozin, V. A. Gasilov, Devender Kumar, J. Nejdli, P. V. Sasorov, Stephen Weber, Daniele Margarone, Yukihiro Kato, G. Korn, H. Kiriya, K. Kondo, Christopher Ridgers, T. Kawachi, Masaki Kando, and Sergei V. Bulanov, "Demonstration of the Brightest Nano-size Gamma Source", *arXiv* **2410.06537**, (2024), DOI: <https://doi.org/10.48550/arXiv.2410.06537>.
15. Stuart Morris, Alex Robinson, and Christopher Ridgers, "Highly efficient conversion of laser energy to hard x-rays in high-intensity laser–solid simulations", *Phys. Plasmas* **28**, 103304 (2021), DOI: <https://doi.org/10.1063/5.0055398>.
16. Sachin Chintalwad, Satheesh Krishnamurthy, Bhu-

- vanesh Ramakrishna, Stuart Morris, and Christopher Ridgers, "Investigation of QED Effects With Varying Z in Thin Foil Targets", *IEEE Transactions On Plasma Science* **49**, 2 (2021) DOI: <https://doi.org/10.1109/TPS.2020.3026781>.
17. Jack Goodman, Martin King, Ewan J. Dolier, Robbie Wilson, Ross J. Gray, and Paul McKenna, "Optimization and control of synchrotron emission in ultraintense laser–solid interactions using machine learning", *High Power Laser Science and Engineering* **11**, 34 (2023), DOI: <https://doi.org/10.1017/hpl.2023.11>.
 18. Sanchin Chintalwad, Satheesh Krishnamurthy, Stuart Morris, Lap Van Dao, and Bhuvanesh Ramakrishna, "Simulation studies of γ -ray radiation in laser-plasma interactions with structured targets", *Fundamental Plasma Physics* **10**, 100038 (2024), DOI: <https://doi.org/10.1016/j.fpp.2024.100038>.
 19. Nathan Smith, Kate Lancaster, Stuart Morris, and Christopher P. Ridgers, "Building robust surrogate models of laser-plasma interactions using large scale PIC simulation", *Plasma Phys. Control. Fusion* **67**, 025013 (2025), DOI: <https://doi.org/10.1088/1361-6587/ada1f5>.
 20. Feng Wan, Chong Lv, Moran Jia, Haibo Sang, and Baisong Xie, "Photon emission by bremsstrahlung and nonlinear Compton scattering in the interaction of ultraintense laser with plasmas", *Eur. Phys. J. D* **71**, 236 (2017), DOI: <https://doi.org/10.1140/epjd/e2017-70805-7>.
 21. Bertrand Martinez, Emmanuel d'Humières, and Laurent Gremillet, "Synchrotron radiation from ultrahigh-intensity laser-plasma interactions and competition with Bremsstrahlung in thin foil targets", *Phys. Rev. Research* **2**, 043341 (2020), DOI: <https://doi.org/10.1103/PhysRevResearch.2.043341>.
 22. Jiří Vyskocil, Evgeny Gelfer, and Ondrej Klimo, "Inverse Compton scattering from solid targets irradiated by ultra-short laser pulses in the 10^{22} – 10^{23} W/cm² regime", *Plasma Phys. Control. Fusion* **62**, 064002 (2020), DOI: <https://doi.org/10.1088/1361-6587/ab83cb>.
 23. Marta Galbiati, Arianna Formenti, Mickael Grech, and Matteo Passoni, "Numerical investigation of non-linear inverse Compton scattering in double-layer targets", *Front. Phys.* **11**, 1117543 (2023). DOI: <https://doi.org/10.3389/fphy.2023.1117543>.
 24. Stuart Morris, 'High-energy X-ray production in laser-solid interactions', PhD. Thesis (University of York, 2022).
 25. Liangliang Ji, Alexander Pukhov, E. N. Nerush, Igor Kostyukov, B. F. Shen, and Kramer Akli, "Energy partition, γ -ray emission, and radiation reaction in the near-quantum electrodynamical regime of laser-plasma interaction", *Phys. Plasmas* **21**, 023109 (2014), DOI: <https://doi.org/10.1063/1.4866014>.
 26. Tony D. Arber, Keith Bennett, Christopher S. Brady, Alistair Lawrence-Douglas, M. G. Ramsay, Nathan J. Sircombe, P. Gillies, Roger G. Evans, Holger Schmitz, Anthony R. Bell, and Christopher P. Ridgers, "Contemporary particle-in-cell approach to laser-plasma modelling", *Plasma Phys. Control. Fusion* **57**, 113001 (2015), DOI: <https://doi.org/10.1088/0741-3335/57/11/113001>.
 27. S. C. Wilks, A. B. Langdon, Thomas E. Cowan, M. Roth, M. Singh, S. Hatchett, M. H. Key, D. Pennington, A. MacKinnon, and R. A. Snavely, "Energetic proton generation in ultra-intense laser–solid interactions", *Phys. Plasmas* **8**, 542–549 (2001), DOI: <https://doi.org/10.1063/1.1333697>.
 28. Stuart Morris, 'Hybrid EPOCH manual', (2022).
 29. Roland Duclous, John G. Kirk, and Anthony R. Bell, "Monte Carlo calculations of pair production in high-intensity laser–plasma interactions", *Plasma Phys. Control. Fusion* **53**, 015009 (2011), DOI: <https://doi.org/10.1088/0741-3335/53/1/015009>.
 30. Christopher P. Ridgers, John G. Kirk, Roland Duclous, Thomas G. Blackburn, Christopher S. Brady, Keith Bennett, Tony D. Arber, and Anthony R. Bell, "Modelling gamma-ray photon emission and pair production in high-intensity laser–matter interactions", *Journal of Computational Physics* **260**, 273–285 (2014) DOI: <https://doi.org/10.1016/j.jcp.2013.12.007>.
 31. Christopher S. Brady, Christopher P. Ridgers, Tony D. Arber, Anthony R. Bell, and John G. Kirk, "Laser Absorption in Relativistically Underdense Plasmas by Synchrotron Radiation", *Phys. Rev. Lett.* **109**, 245006 (2012), DOI: <https://doi.org/10.1103/PhysRevLett.109.245006>.
 32. Kirill Lezhnin, Pavel Sasorov, Georg Korn, and Sergei Bulanov, "High power gamma flare generation in multi-petawatt laser interaction with tailored targets", *Phys. Plasmas* **25**, 123105 (2018), DOI: <https://doi.org/10.1063/1.5062849>.
 33. X. B. Wang, G. Y. Hu, Z. M. Zhang, Y. Q. Gu, B. Zhao, Y. Zuo, and J. Zheng, "Gamma-ray generation from ultraintense laser-irradiated solid targets with preplasma", *High Power Laser Science and Engineering* **8**, 34 (2020), DOI: <https://doi.org/10.1017/hpl.2020.30>.
 34. Tatsufumi Nakamura, James K. Koga, Timur Zh. Esirkepov, Masaki Kando, Georg Korn, and Sergei V. Bulanov, "High-Power γ -Ray Flash Generation in Ultraintense Laser-Plasma Interactions", *Phys. Rev. Lett.* **108**, 195001 (2012), DOI: <https://doi.org/10.1103/PhysRevLett.108.195001>.
 35. H. X. Chang, Bingqiang Qiao, Yu-Xiang Zhang, Zhihao Xu, Wei-Ming P. Yao, C. T. Zhou, and Xian-Tu He, "Brilliant petawatt gamma-ray pulse generation in quantum electrodynamic laser-plasma interaction", *Phys. Plasmas* **27**, 043111 (2017), DOI: <https://doi.org/10.1063/1.4866014>.

10.1038/srep45031.

36. Prokopis Hadjisolomou, Tae Moon Jeong, David Kolenaty, Alexander J. Macleod, Veronica Olšovcová, Roberto Versaci, Christopher P. Ridgers, Sergei V. Bulanov, "Gamma-flash generation in multi-petawatt laser-matter interactions", *Phys. Plasmas* **30**, 093103 (2023), DOI: <https://doi.org/10.1063/5.0158264>.